

MedVKAN: Efficient Feature Extraction with Mamba and KAN for Medical Image Segmentation

Hancan Zhu¹, Jinhao Chen¹ and Guanghua He^{1,*}

¹ School of Mathematics, Physics and Information, Shaoxing University, Shaoxing, Zhejiang, 312000, China

*Corresponding author:

Guanghua He, 900 ChengNan Rd, School of Mathematics Physics and Information, Shaoxing University, Shaoxing, Zhejiang, China 312000. Email: hegh23@sina.com

Abstract

Medical image segmentation relies heavily on convolutional neural networks (CNNs) and Transformer-based models. However, CNNs are constrained by limited receptive fields, while Transformers suffer from scalability challenges due to their quadratic computational complexity. To address these limitations, recent advances have explored alternative architectures. The state-space model Mamba offers near-linear complexity while capturing long-range dependencies, and the Kolmogorov-Arnold Network (KAN) enhances nonlinear expressiveness by replacing fixed activation functions with learnable ones. Building on these strengths, we propose MedVKAN, an efficient feature extraction model integrating Mamba and KAN. Specifically, we introduce the EFC-KAN module, which enhances KAN with convolutional operations to improve local pixel interaction. We further design the VKAN module, integrating Mamba with EFC-KAN as a replacement for Transformer modules, significantly improving feature extraction. Extensive experiments on five public medical image segmentation datasets show that MedVKAN achieves state-of-the-art performance on four datasets and ranks second on the remaining one. These results validate the potential of Mamba and KAN for medical image segmentation while introducing an innovative and computationally efficient feature extraction framework. The code is available at: <https://github.com/beginner-cjh/MedVKAN>.

Keywords: Medical Image Segmentation; Mamba; Kolmogorov-Arnold Network; Transformer

1 Introduction

Medical image segmentation plays a crucial role in modern clinical practice, with widespread applications in assisted diagnosis, treatment planning, and therapeutic outcome evaluation [1-3]. It facilitates precise identification and quantification of pathological regions, providing essential guidance for surgical planning and treatment monitoring. However, traditional segmentation methods rely heavily on manual annotation and expert interpretation, making them time-consuming, labor-intensive, and susceptible to inter-observer variability, which can compromise diagnostic consistency [4, 5]. To address these limitations, deep learning-based automated segmentation methods have emerged as a transformative technology, offering enhanced efficiency, accuracy, and reproducibility [6, 7].

Deep learning techniques, particularly convolutional neural networks (CNNs) and Transformer-based models, have led to significant advancements in medical image segmentation [8-11]. CNN-based architectures, such as U-Net [8], ResNet [12], nnU-Net [9], and SegResNet [13], leverage weight sharing and pooling mechanisms to efficiently extract local features, making them well-suited for processing

medical images. However, their reliance on local operations inherently limits their ability to model long-range dependencies. In contrast, Transformer-based models, including SwinTransformer [14], UNETR [15], SwinUNETR [16], employ multi-head self-attention (MHSA) mechanisms to capture global dependencies effectively. Despite their superior global feature extraction capabilities, their quadratic computational complexity significantly increases the cost of processing high-resolution medical images.

In recent years, state-space models (SSMs) [19, 20] have been widely applied in computer vision. Among them, Mamba [21], a recently proposed SSM, has attracted significant attention due to its strong global feature extraction capability combined with near-linear computational complexity. As a result, many researchers have compared Mamba with Transformers, and it has demonstrated competitive performance in fields such as natural language processing and medical image analysis [22-26]. For instance, U-Mamba [23] introduced a hybrid module within the nnU-Net framework [9], integrating CNN’s local feature extraction with Mamba’s global modeling ability, marking an initial exploration of Mamba blocks in medical image analysis. VMamba [24] further enhanced Mamba’s capability by introducing the SS2D module, which traverses images along four scanning paths, addressing the misalignment between one-dimensional sequential scanning and the non-sequential nature of two-dimensional visual data, thereby capturing contextual information from multiple perspectives. Swin-UMamba [25] extended U-Mamba and VMamba by investigating ImageNet-pretrained Mamba models for medical image segmentation. Additionally, SegMamba [26] proposed a three-directional spatial Mamba module, which unfolds images along three axes to improve 3D sequential modeling. It also introduced a gated spatial convolution module to enhance spatial feature extraction, further improving segmentation performance.

Meanwhile, Kolmogorov-Arnold Networks (KANs) [27, 28], grounded in the Kolmogorov-Arnold representation theorem [29, 30], have demonstrated exceptional nonlinear expressiveness by parameterizing B-spline functions. In tasks such as data fitting and solving partial differential equations, KANs significantly outperform multi-layer perceptrons (MLPs) while requiring substantially fewer parameters. The potential of KANs has also been extensively explored in computer vision. For instance, UKAN [31] incorporated Tok-KAN as a feature extractor within the U-Net framework, providing initial evidence of KAN’s effectiveness in medical image segmentation. KAT [32] introduced GR-KAN, which replaces B-spline functions with rational functions and integrates KAN with Transformers, effectively mitigating KAN’s computational inefficiencies. Conv-KAN [33] proposed a KAN-based convolutional layer, where convolutional kernels are parameterized using learnable B-spline interpolation functions, reducing parameter complexity while maintaining high accuracy. Furthermore, TransUKAN [34] introduced EfficientKAN, which integrates KAN with Transformers to leverage KAN’s local nonlinear modeling capabilities, further optimizing Transformer architecture and performance.

Given the significant advantages of Mamba and KAN modules in feature extraction, prior studies have investigated replacing MHSA blocks with Mamba blocks [26] and substituting MLP blocks with KAN blocks [32, 34]. However, the integration of Mamba and KAN remains largely unexplored. Effectively leveraging their complementary strengths to enhance feature extraction and overall model performance remains a challenging research problem. To address this gap, we propose MedVKAN, an efficient feature extraction model for medical image segmentation that synergistically integrates Mamba and KAN within a U-Net-inspired framework. MedVKAN adopts a multi-stage encoder-decoder architecture with skip connections, designed to balance local and global feature extraction. Specifically, convolutional layers are utilized in the first three encoder stages to effectively capture local features, while the last two encoder stages incorporate the proposed VKAN block to extract global features,

enabling an optimal trade-off between segmentation performance and computational efficiency. The primary contributions of this study are as follows:

- We integrate Mamba and KAN into the VKAN block as a potential alternative to Transformer architecture, leveraging Mamba's global feature extraction and KAN's nonlinear expressiveness to enhance image feature extraction.
- To improve information interaction among adjacent pixels, we incorporate two additional 3×3 convolutions before the KAN module. This design effectively strengthens feature representation within the model.
- Extensive experiments on five public datasets demonstrate that MedVKAN achieves state-of-the-art performance on four datasets and ranks second on the remaining one, highlighting its effectiveness, robustness, and broad applicability in medical image segmentation.

2 Method

As illustrated in Figure 1, the proposed MedVKAN model comprises three main components: the encoder, the decoder, and skip connections. The encoder consists of three convolutional blocks, two VKAN blocks specifically designed in this work, as well as Patch Embedding [11] and Patch Merging [14] operations. The decoder adopts a structure similar to the encoder, aiming to progressively restore the spatial resolution of feature maps. The skip connections integrate low-level features from the encoder with high-level abstract features from the decoder, preserving fine-grained details while restoring spatial resolution. To further enhance segmentation performance, a deep supervision mechanism is incorporated, enabling auxiliary predictions at multiple scales [35].

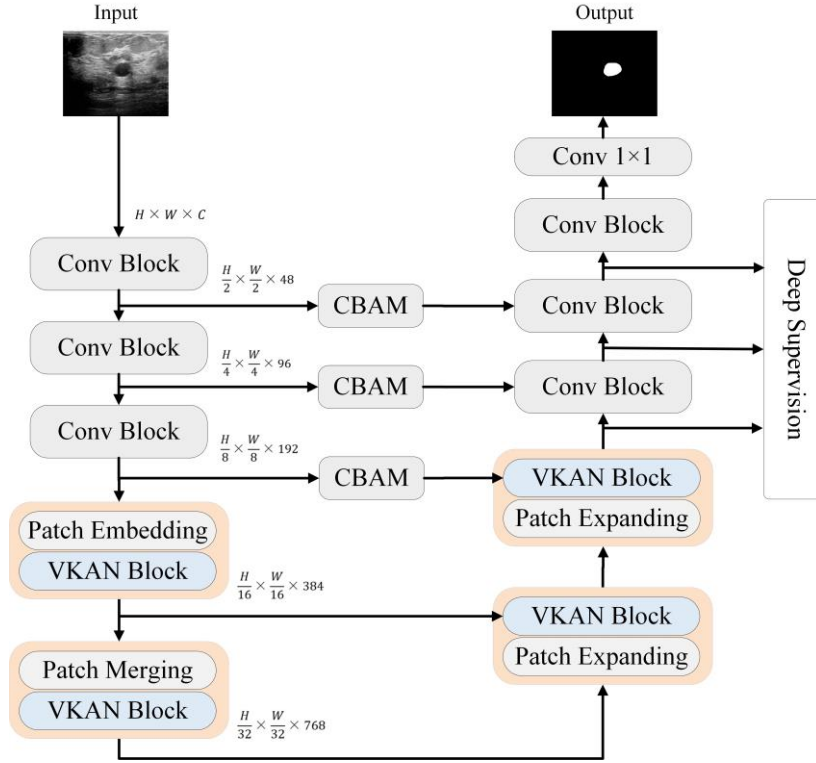


Figure 1. Schematic of the MedVKAN framework, comprising an encoder, decoder, and skip connections. It integrates convolutional blocks, VKAN blocks, and CBAM modules to enhance feature representation and segmentation performance.

2.1 Feature Extraction in MedVKAN

Given an input image $I \in \mathbb{R}^{B \times C \times H \times W}$, where B denotes the batch size, C represents the number of channels, and H and W correspond to the height and width of the input image, respectively. The feature extraction process is primarily divided into three components: the encoder, skip connections, and the decoder, as detailed below.

In the encoder, the input image first passes through the initial convolutional block for preliminary feature extraction, producing a feature map $x_{e,1} \in \mathbb{R}^{B \times 48 \times \frac{H}{2} \times \frac{W}{2}}$. Subsequently, the feature map is processed through the second and third convolutional blocks, extracting progressively deeper features and generating feature maps $x_{e,2} \in \mathbb{R}^{B \times 96 \times \frac{H}{4} \times \frac{W}{4}}$ and $x_{e,3} \in \mathbb{R}^{B \times 192 \times \frac{H}{8} \times \frac{W}{8}}$, respectively. Here, $x_{e,i}$ represents the output feature map at the i -th stage of the encoder. Each convolutional block comprises two consecutive 3×3 convolution operations followed by a max pooling (MP) operation for downsampling. The computation process is formulated as follows:

$$\begin{aligned}\bar{x}_{e,i+1} &= \text{ReLU}(\text{BN}(\text{Conv}(x_{e,i}))), \\ x_{e,i+1} &= \text{MP}\left(\text{ReLU}\left(\text{BN}\left(\text{Conv}(\bar{x}_{e,i+1})\right)\right)\right).\end{aligned}$$

Here, Conv denotes 3×3 convolution operation, BN represents batch normalization, and ReLU is the activation function.

Next, the feature map $x_{e,3}$ undergoes downsampling via Patch Embedding, which applies a 2×2 convolution with a stride of 2 to reduce spatial resolution while increasing the channel dimension. The resulting feature map is then processed by a VKAN block, yielding $x_{e,4} \in \mathbb{R}^{B \times \frac{H}{16} \times \frac{W}{16} \times 384}$. Subsequently, Patch Merging partitions the feature map into four regions and concatenates them along the channel dimension, producing a feature map of shape $B \times \frac{H}{32} \times \frac{W}{32} \times 1536$. A linear projection then reduces the channel dimension to 768, followed by another VKAN block, generating the final encoder output $x_{e,5} \in \mathbb{R}^{B \times \frac{H}{32} \times \frac{W}{32} \times 768}$. The VKAN block is described in detail in Section 2.2.

In the skip connections, we introduce the CBAM module [36] to enhance the feature maps $x_{e,1}$, $x_{e,2}$, and $x_{e,3}$ from the first three encoder stages by refining salient information across both channel and spatial dimensions. The refined feature maps, denoted as s_1, s_2 and s_3 , are then utilized for feature fusion in the decoding process. A detailed explanation of the CBAM module is provided in Section 2.3.

The decoder is designed symmetrically to the encoder. First, the encoded feature map $x_{e,5}$ is upsampled using Patch Expanding [37], where a linear projection initially maps it to $R^{B \times \frac{H}{32} \times \frac{W}{32} \times 1536}$, followed by a rearrange operation that reshapes it into $R^{B \times \frac{H}{16} \times \frac{W}{16} \times 384}$. The resulting feature map is then concatenated along the channel dimension with the feature map $x_{e,4}$ transmitted through the skip connection. To ensure compatibility, a 1×1 convolution restores the channel dimension to 384, followed by processing through a VKAN block, yielding $x_{d,5} \in \mathbb{R}^{B \times \frac{H}{16} \times \frac{W}{16} \times 384}$.

This process is iteratively applied, producing $x_{d,4} \in \mathbb{R}^{B \times \frac{H}{8} \times \frac{W}{8} \times 192}$. Next, three convolutional blocks further refine the features while progressively restoring spatial resolution, generating the feature maps $x_{d,3} \in \mathbb{R}^{B \times 96 \times \frac{H}{4} \times \frac{W}{4}$, $x_{d,2} \in \mathbb{R}^{B \times 48 \times \frac{H}{2} \times \frac{W}{2}}$ and $x_{d,1} \in \mathbb{R}^{B \times 24 \times H \times W}$. Finally, a 1×1 convolution performs channel compression, producing the final segmentation output.

2.2 VKAN Block

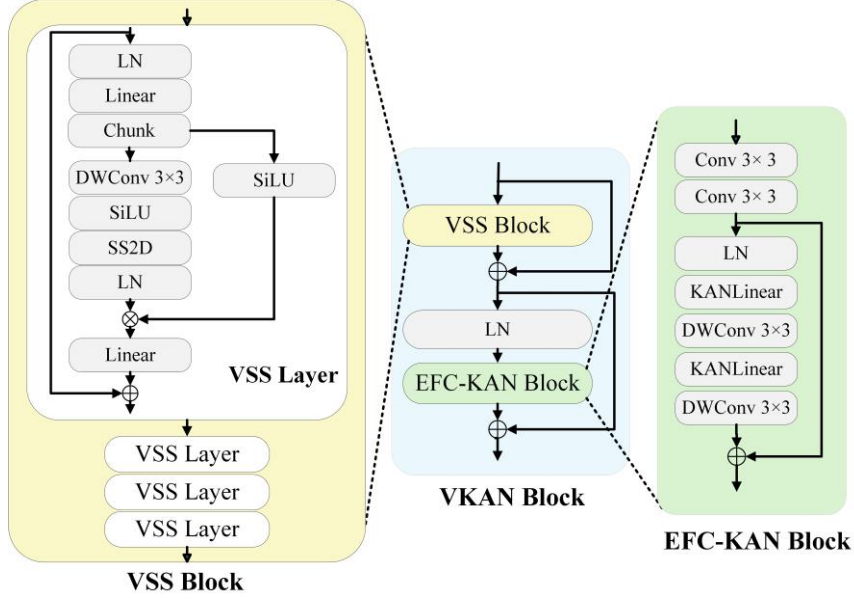


Figure 2. Structural diagram of the VKAN block. The input feature map is sequentially processed through the VSS block, Layer Normalization (LN), and the EFC-KAN block, with a residual connection facilitating element-wise addition to enhance feature preservation.

In MedVKAN, we introduce the VKAN block as a replacement for the Transformer block, integrating a VSS block and an EFC-KAN block to enhance global feature extraction and nonlinear representation while reducing computational complexity. As shown in Figure 2, the VKAN module first processes input features through the VSS block, followed by a residual connection and Layer Normalization (LN). The transformed features then pass through the EFC-KAN block, with an additional residual connection further refining the module's output.

2.2.1 VSS Block

As shown in Figure 2, the VSS block consists of four VSS layers, an improved version of Mamba, each designed based on [24]. Given an input feature map $x \in \mathbb{R}^{B \times H \times W \times C}$, the process begins with LN, followed by a linear projection that expands the channel dimension to $4C$, producing $\bar{x} \in \mathbb{R}^{B \times H \times W \times 4C}$. The expanded feature map is then split along the channel dimension into two components, $\bar{x}_1, \bar{x}_2 \in \mathbb{R}^{B \times H \times W \times 2C}$, using a chunking operation.

For feature extraction, \bar{x}_1 is first permuted to $\mathbb{R}^{B \times 2C \times H \times W}$ and sequentially processed by depthwise convolution (DWConv), SiLU activation, and the 2D Selective Scanning (SS2D) module to enhance spatial feature representation. The output is then reshaped back to $\mathbb{R}^{B \times H \times W \times 2C}$ and normalized. Next, the refined \bar{x}_1 is element-wise multiplied with the SiLU-activated \bar{x}_2 , yielding the updated feature representation $\bar{x} \in \mathbb{R}^{B \times H \times W \times 2C}$. To restore the original channel dimension, a linear projection

maps \bar{x} back to $\mathbb{R}^{B \times H \times W \times C}$. Finally, a residual connection adds \bar{x} to the original input x , ensuring stable feature propagation and enhancing representational capacity.

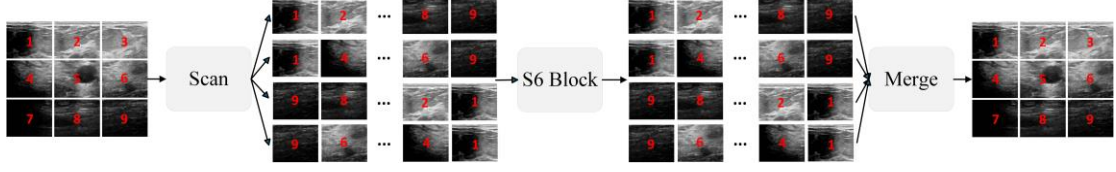


Figure 3. Schematic illustration of the 2D Selective Scanning (SS2D) module, which consists of three main components: the Cross-Scanning Block (Scan), the S6 Block, and the Cross-Merging Block (Merge).

As illustrated in Figure 3, the SS2D module consists of three main components: the Cross-Scanning Block (Scan), the S6 Block, and the Cross-Merging Block (Merge). The Cross-Scanning Block first scans the input feature map in four directions: left to right, top to bottom, right to left, and bottom to top, generating four sequential feature representations. Each sequence captures direction-specific contextual information, enabling a more comprehensive understanding of global dependencies within the feature map. These sequential features are then processed by the S6 Block for feature extraction. The S6 Block employs a state update mechanism, where the input sequence $x(t)$ is integrated with the hidden state $h(t)$ and mapped to the output $y(t)$ using the following equations:

$$\begin{aligned} h'(t) &= \mathbf{A}h(t) + \mathbf{B}x(t), \\ y(t) &= \mathbf{C}h(t), \end{aligned}$$

where, $\mathbf{A} \in \mathbb{R}^{N \times N}$, $\mathbf{B} \in \mathbb{R}^{N \times 1}$, and $\mathbf{C} \in \mathbb{R}^{1 \times N}$ are learnable parameter matrices. Here, \mathbf{A} governs the temporal evolution of the hidden state $h(t)$, \mathbf{B} determines the influence of the input $x(t)$ on the updated hidden state $h'(t)$, and \mathbf{C} maps the hidden state $h(t)$ to the output $y(t)$.

2.2.2 EFC-KAN Block

The EFC-KAN block builds on KAN, which parameterizes learnable basis functions using B-splines. The k -th order spline basis function at the i -th channel is computed as:

$$N_{i,k}(x_l) = \frac{x_l - t_i}{t_{i+k} - t_i} N_{i,k-1}(x_l) + \frac{t_{i+k+1} - x_l}{t_{i+k+1} - t_{i+1}} N_{i+1,k-1}(x_l),$$

where, $N_{i,k}(x_l)$ represents the k -th order basis function at the i -th channel, t_i is the node at the i -th channel, and x_l corresponds to the l -th pixel in the input feature map along the sequence dimension. However, because spline basis functions at each sequence position rely only on local input, spatial information exchange is limited, potentially hindering feature extraction. To address this, we introduce Expanded Field Convolution (EFConv) before the KAN block, forming the EFC-KAN block. EFConv comprises two 3×3 convolutional layers that expand the receptive field and enhance spatial information interaction.

The KAN block consists of two layers of KANLinear and DWConv, collectively referred to as the Tok-KAN block [31]. KANLinear, the core component of KAN, leverages B-spline functions to enable learnable weight representations. Its design is based on the Kolmogorov-Arnold theorem [29, 30], which states that any continuous function can be expressed as a composition of a finite number of continuous univariate functions. The KANLinear transformation is defined as:

$$\Phi(x) = \begin{pmatrix} \phi_{1,1}(\cdot) & \cdots & \phi_{1,n}(\cdot) \\ \vdots & \ddots & \vdots \\ \phi_{m,1}(\cdot) & \cdots & \phi_{m,n}(\cdot) \end{pmatrix} x,$$

where $\phi_{m,n}(\cdot)$ represents a learnable univariate function, and m and n denote the output and input feature dimensions, respectively.

The EFC-KAN block follows a three-step computation process:

(1) The input feature map undergoes two consecutive 3×3 convolutions, enhancing spatial information interaction:

$$\bar{x} = EFConv(x) = Conv(Conv(x)).$$

(2) The EFConv output \bar{x} is processed by the Tok-KAN block, formulated as:

$$Tok_{KAN}(\bar{x}) = DWConv\left(KANLinear\left(DWConv\left(KANLinear(LN(\bar{x}))\right)\right)\right).$$

(3) The final output is obtained via a residual connection:

$$EFC_{KAN}(\bar{x}) = Tok_{KAN}(\bar{x}) + \bar{x}.$$

By incorporating EFConv and Tok-KAN, the EFC-KAN block enhances spatial information interaction and nonlinear feature modeling, significantly improving feature extraction efficiency.

2.3 CBAM Block

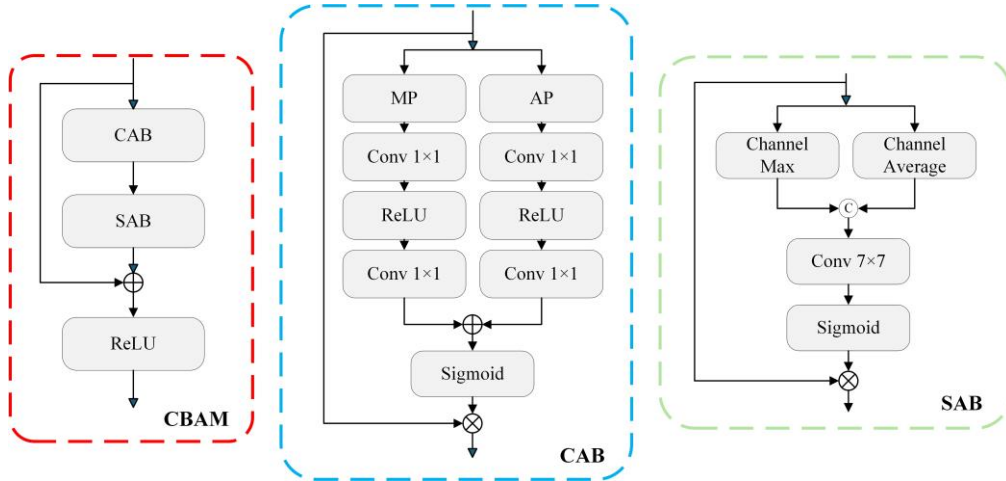


Figure 4. Schematic diagram of the CBAM structure, consisting of a Channel Attention Block (CAB) and a Spatial Attention Block (SAB).

The CBAM block enhances feature representation by sequentially refining the input feature map along the channel and spatial dimensions. As shown in Figure 4, the feature map first passes through the Channel Attention Block (CAB), which extracts channel-wise attention. CAB utilizes max pooling (MP) and average pooling (AP) along the spatial dimension in parallel branches to generate channel descriptors. These descriptors are processed by a convolutional layer for dimensionality reduction, followed by ReLU activation, and then another convolutional layer restores the original channel dimension. The outputs are summed and passed through a Sigmoid activation function to produce channel attention scores, which are applied via channel-wise multiplication to enhance the feature representation.

After channel refinement, the Spatial Attention Block (SAB) further enhances the feature map. It applies max pooling and average pooling along the channel dimension, concatenating the results to form

a spatial descriptor. A 7×7 convolutional layer extracts spatial dependencies while reducing the channel dimension to 1. The output is then activated by Sigmoid, generating spatial attention scores, which are applied via element-wise multiplication to emphasize spatially significant features.

Finally, a residual connection adds the refined feature map to the original input, followed by ReLU activation, enhancing feature propagation and representational capacity.

2.4 Loss Function

Our network employs a deep supervision mechanism, where the total loss is a weighted sum of Dice loss and cross-entropy loss across multiple decoding stages:

$$Total\ Loss = \sum_{k=1}^4 \alpha_k Loss_k, \text{ with } Loss_k = DiceLoss_k + CrossEntropyLoss_k.$$

The Dice loss at stage k is defined as:

$$DiceLoss_k = 1 - \frac{2|Y \cap \tilde{Y}^k|}{|Y| + |\tilde{Y}^k|}.$$

The cross-entropy loss at stage k is given by:

$$CrossEntropyLoss_k = -\frac{1}{N} \sum_{i=1}^N \sum_{j=1}^C y_{ij} \log p_{ij}^k.$$

In the above formulas, Y represents the ground truth segmentation mask, and \tilde{Y}^k denotes the predicted segmentation mask at stage k . N is the total number of pixels, and C is the number of segmentation classes. The term y_{ij} is the one-hot encoded ground truth label for pixel i in class j , while p_{ij}^k represents the predicted probability of pixel i belonging to class j at stage k . The weighting coefficients $\alpha_1, \alpha_2, \alpha_3, \alpha_4$ are set to 1.0, 0.5, 0.25, and 0.125, respectively, corresponding to the four decoder stages. The first stage provides the final segmentation result, while the remaining stages contribute to feature refinement through deep supervision.

3 Experiments and Results

3.1 Datasets

We performed comprehensive experiments on five publicly available medical image segmentation datasets, covering a diverse range of segmentation tasks, including cell instance segmentation, multi-organ abdominal segmentation, breast cancer lesion segmentation, multi-class cardiac segmentation, and COVID-19 infection segmentation. The datasets encompass various imaging modalities, including microscopy, magnetic resonance imaging (MRI), ultrasound, and computed tomography (CT).

The Microscopy dataset originates from the NeurIPS 2022 Cell Segmentation Challenge [38], which focuses on cell segmentation across various microscopy images. Cell segmentation is a fundamental step in the quantitative analysis of individual cells in microscopic images. This dataset is specifically designed for instance segmentation, with images cropped to a resolution of (512, 512) for both training and testing. It comprises 1000 images for training and 101 images for testing. To ensure consistency, we adopted the same data preprocessing strategy as described in [23].

The Abdomen MRI dataset originates from the MICCAI 2022 AMOS Challenge [39], which focuses on segmenting 13 abdominal organs from MRI scans, including the liver, spleen, pancreas, right

kidney, left kidney, stomach, gallbladder, esophagus, aorta, inferior vena cava, right adrenal gland, left adrenal gland, and duodenum. Following the experimental setup in [23], we incorporated an additional 50 MRI scans for testing. Specifically, the dataset comprises 60 MRI scans with 5615 slices for training and 50 MRI scans with 3357 slices for testing. All images were cropped to a resolution of (320, 320) for both training and testing.

The BUSI dataset was collected in 2018 by Walid Al-Dhabyani et al. from Cairo University, Egypt [40]. It comprises ultrasound images of normal, benign, and malignant breast cancer cases, along with their corresponding segmentation masks. For our study, we utilized all ultrasound images representing benign and malignant breast cancer cases, totaling 647 images. The images were resized to (512, 512) for both training and testing, with 517 images allocated for training and 130 for testing.

The ACDC dataset originates from the Automated Cardiac Diagnosis Challenge (ACDC) [41]. It consists of MRI scans from 150 patients, with each patient having two different MRI modalities. This challenge aims to segment the left ventricle, right ventricle, and myocardium from MRI scans. For our study, we utilized the training subset of the original dataset, which includes MRI scans from 100 patients. We further split this subset into training and testing sets using an 8:2 ratio, resulting in 160 MRI scans from 80 patients for training and 40 MRI scans from 20 patients for testing. All images were resized to (256, 256) for both training and testing.

The COVID-19 dataset was constructed by MS-Net [42] through the integration of publicly available datasets, including the dataset from [<https://medicalsegmentation.com/COVID19/>] and another publicly available dataset [43]. Uniform sampling was applied to obtain a total of 1277 high-quality CT images, with 894 images designated for training and 383 for testing. All images were resized to (512, 512) for both training and testing.

3.2 Implementation Details

We trained MedVKAN using the nnU-Net framework [9], which automates hyperparameter configuration and data preprocessing. This automation allowed us to focus on model architecture design while maintaining the flexibility to adjust hyperparameters when needed. Additionally, leveraging this framework ensured a fair comparison with other models under similar configurations. All experiments were conducted on a single NVIDIA GeForce RTX 4090D GPU. The initial learning rate was set to 0.0002, with a batch size of 8. We employed the AdamW optimizer with a weight decay of 0.05. The learning rate followed a cosine annealing schedule, with a minimum value of 0.000001. The model was trained for 1000 epochs.

3.3 Compared Models and Evaluation Metrics

We conducted comparative experiments using six models across four categories: traditional CNNs (nnU-Net [9], SegResNet [13]), Transformer-based models (UNETR [15], SwinUNETR [16]), a Mamba-based model (Swin-UMamba [25]), and a KAN-based model (UKAN [31]). To ensure a fair comparison, all methods were implemented within the nnU-Net framework, with hyperparameters set according to their original studies. For consistency, all models were trained from scratch for 1000 epochs under the same experimental conditions.

Following [44], we employed the Dice similarity coefficient and normalized surface distance (NSD) to evaluate segmentation performance on the two MRI-based datasets: Abdomen MRI and ACDC. Since the Microscopy dataset involves cell instance segmentation, we used the F1-score to assess cell segmentation quality. For the BUSI and COVID-19 datasets, we adopted intersection over union (IoU)

and Dice similarity coefficient as evaluation metrics. The definitions of these metrics are as follows:

$$\begin{aligned}
Dice &= \frac{2|Y \cap \tilde{Y}|}{|Y| + |\tilde{Y}|}, \\
NSD &= \frac{|S_{pred} \cap S_{gt,\tau}| + |S_{gt} \cap S_{pred,\tau}|}{|S_{pred}| + |S_{gt}|}, \\
IoU &= \frac{|Y \cap \tilde{Y}|}{|Y \cup \tilde{Y}|}, \\
F1 &= 2 \times \frac{Precision \times Recall}{Precision + Recall}, \text{ if } IoU > 0.5, \\
Precision &= \frac{TP}{TP + FP}, \\
Recall &= \frac{TP}{TP + FN}.
\end{aligned}$$

In the above formulas, Y represents the ground truth segmentation mask, while \tilde{Y} denotes the predicted segmentation mask. S_{pred} and S_{gt} represent the surface point sets of the predicted and ground truth segmentations, respectively. $S_{pred,\tau}$ consists of predicted surface points whose shortest distance to the ground truth surface is within the threshold τ , whereas $S_{gt,\tau}$ includes ground truth surface points whose shortest distance to the predicted surface is within the threshold τ . In cell instance segmentation, a segmentation is considered accurate if its IoU with the ground truth exceeds 0.5. The F1-score is then computed based on this criterion. True positives (TP) are correctly classified foreground pixels, false positives (FP) are background pixels mistakenly classified as foreground, and false negatives (FN) are foreground pixels that were misclassified as background.

3.4 Experimental Results

Table 1. Experimental results of different models on the Microscopy, BUSI, and Abdomen MRI datasets. The best-performing model is highlighted in bold, while the second-best is underlined. Results for nnU-Net, SegResNet, UNETR, and SwinUNETR on the Microscopy and Abdomen MRI datasets are sourced from [23]. The parameter count and computational cost for the BUSI dataset are consistent with those of the Microscopy dataset.

Methods	Microscopy			BUSI		Abdomen MRI			
	#Params	#FLOPs	F1	IoU	Dice	#Params	#FLOPs	Dice	NSD
nnU-Net	46M	59.0G	0.538	0.680	0.763	33M	23.0G	0.745	0.815
SegResNet	6M	62.4G	<u>0.541</u>	0.653	0.743	6M	24.3G	0.732	0.803
UNETR	88M	105.6G	0.436	0.597	0.695	87M	41.0G	0.575	0.631
SwinUNETR	25M	75.7G	0.397	0.671	0.762	25M	29.4G	0.703	0.767
Swin-UMamba	59M	160.8G	0.492	<u>0.699</u>	<u>0.783</u>	59M	62.7G	<u>0.754</u>	<u>0.820</u>
UKAN	25M	27.4G	0.529	0.664	0.750	25M	10.7G	0.730	0.797
MedVKAN	51M	56.5G	0.604	0.709	0.788	51M	22.0G	0.762	0.830

Table 2. Experimental results of different models on the ACDC and COVID-19 datasets. The best-performing model is highlighted in bold, while the second-best is underlined.

Methods	ACDC				COVID-19			
	#Params	#FLOPs	Dice	NSD	#Params	#FLOPs	IoU	Dice
nnU-Net	20M	14.7G	0.913	0.974	46M	59.0G	0.620	0.688

SegResNet	6M	15.5G	<u>0.916</u>	<u>0.980</u>	6M	62.2G	0.612	0.682
UNETR	87M	26.2G	0.869	0.938	87M	105.1G	0.596	0.667
SwinUNETR	25M	19.0G	0.908	0.971	25M	75.4G	0.612	0.680
Swin-UMamba	59M	40.0G	0.912	0.971	59M	160.2G	0.635	0.701
UKAN	25M	6.8G	0.913	0.977	25M	27.2G	0.602	0.668
MedVKAN	51M	14.0G	0.922	0.981	51M	56.2G	<u>0.630</u>	<u>0.696</u>

As shown in Table 1, MedVKAN achieves the highest F1-score on the Microscopy dataset, exceeding the second-best model by 6%. Since the F1-score is computed only for instances with IoU > 0.5, a higher score suggests that MedVKAN segments more instances with sufficient accuracy, reflecting superior segmentation completeness and recall. On the BUSI dataset, MedVKAN outperforms Swin-UMamba, the second-best model, with a 1% higher IoU and a 0.5% higher Dice score, demonstrating enhanced segmentation accuracy and robustness. Similarly, on the Abdomen MRI dataset, MedVKAN surpasses the second-best model by 0.8% in Dice score and 1% in NSD, further improving segmentation precision and boundary delineation.

Table 2 further highlights MedVKAN’s strong performance on the ACDC dataset, where all models achieve relatively high accuracy. MedVKAN outperforms the second-best model by 0.6% in Dice score and 0.1% in NSD, demonstrating its robustness in cardiac segmentation. On the COVID-19 dataset, although MedVKAN ranks second overall, it maintains a notable advantage over most models, reaffirming its effectiveness in infection region segmentation. These results collectively emphasize MedVKAN’s capability to deliver accurate and reliable segmentation across diverse datasets. Furthermore, as evidenced in Tables 1 and 2, while MedVKAN does not have an advantage in parameter count, it exhibits superior computational efficiency, particularly when compared to Transformer-based models.

Figure 5 provides a visual comparison of segmentation results. On the Microscopy dataset (row a), Swin-UMamba and UKAN struggle to distinguish boundaries between nearly overlapping cells, whereas MedVKAN effectively resolves this challenge, achieving more complete segmentation. Similarly, on the Abdomen MRI dataset (row b), MedVKAN demonstrates higher accuracy in delineating closely overlapping organ boundaries. Figure 6 further highlights MedVKAN’s consistency across different datasets. On the BUSI dataset (row a), it produces smoother breast cancer segmentations, while Transformer-based models tend to introduce noise. For the ACDC dataset (row b), MedVKAN achieves more precise segmentation of the left ventricle, right ventricle, and myocardium. On the COVID-19 dataset (row c), although it does not achieve the highest ranking, MedVKAN maintains upper mid-tier segmentation accuracy, demonstrating strong overall competitiveness.

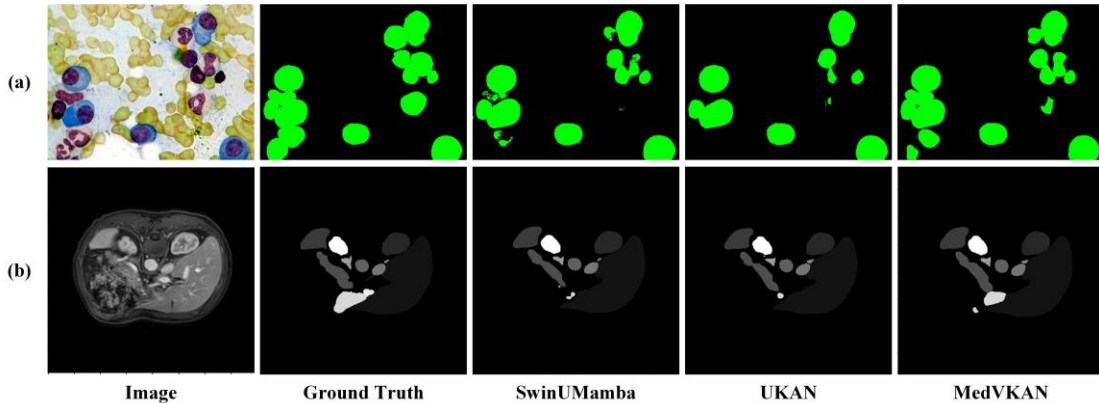


Figure 5. Visualization of segmentation results from different models on the Microscopy and Abdomen MRI datasets. Row (a) presents results for the Microscopy dataset, while row (b) shows results for the Abdomen MRI dataset.

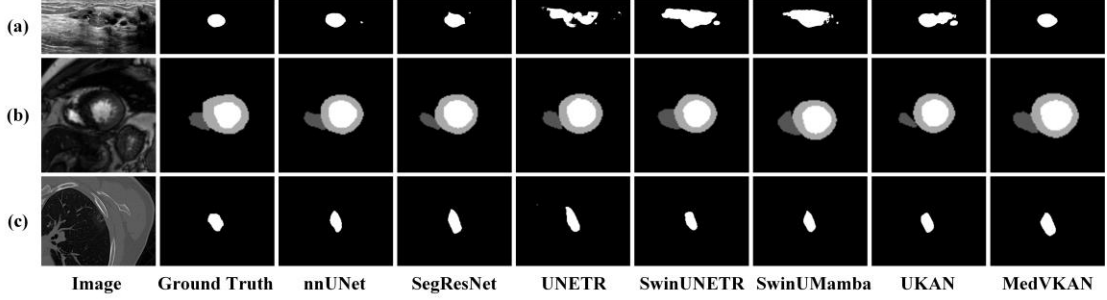


Figure 6. Visualization of segmentation results from different models on the BUSI, ACDC, and COVID-19 datasets. Row (a) corresponds to the BUSI dataset, row (b) to the ACDC dataset, and row (c) to the COVID-19 dataset. To enhance visibility, images in rows (b) and (c) have been resized and cropped due to the small segmentation regions.

3.5 Ablation Study

Our VKAN block follows an architecture similar to the Transformer block. To evaluate its effectiveness, we first compare the VKAN block with the Transformer block through an ablation study, as summarized in Table 3. In this comparison, "MHSA+MLP" represents the standard Transformer architecture, "VSS+MLP" replaces the MHSA block with the VSS block, "MHSA+EFC-KAN" substitutes the MLP block with the EFC-KAN block, and "VSS+EFC-KAN" corresponds to our proposed model. The results demonstrate that our model achieves the best performance by effectively leveraging the complementary strengths of Mamba and KAN.

To further investigate the impact of convolutional kernel sizes in EFConv on EFC-KAN's feature extraction, we conducted an additional ablation study, as shown in Table 4. In this study, "Conv3×3" applies a single 3×3 convolution to expand the receptive field, "Conv5×5" uses a single 5×5 convolution, and "2*Conv3×3" stacks two 3×3 convolutions to achieve an equivalent receptive field to "Conv5×5". The results indicate that while the "Conv3×3" significantly enhances performance, the "Conv5×5" provides further improvements. Notably, "2*Conv3×3" achieves comparable or superior performance to "Conv5×5" while reducing parameter count and computational complexity, making it the optimal choice.

Table 3. Ablation study of the VKAN block architecture on the BUSI dataset.

Components				Metrics	
VSS	MHSA	EFC-KAN	MLP	IoU	Dice
×	√	×	√	0.607	0.702
√	×	×	√	0.690	0.768
×	√	√	×	0.663	0.759
√	×	√	×	0.709	0.788

Table 4. Ablation study on the selection of convolutional blocks in EFConv on the BUSI dataset.

Components			Metrics	
Conv3 × 3	Conv5 × 5	2 * Conv3 × 3	IoU	Dice
×	×	×	0.677	0.757

√	×	×	0.698	0.777
×	√	×	0.702	0.783
×	×	√	0.709	0.788

4 Conclusion and future work

This study introduces MedVKAN, a model that combines U-Net’s feature extraction capabilities with Mamba’s global modeling strengths, further enhanced by the EFC-KAN module. This work serves as a preliminary investigation into the potential joint application of Mamba and KAN for medical image segmentation. Experimental results indicate that MedVKAN delivers competitive performance across diverse medical imaging modalities and tasks. However, further optimization is needed, particularly in reducing computational overhead and improving scalability for large-scale datasets. Future research will focus on developing lightweight architectures and efficient training strategies to enhance performance while maintaining computational feasibility. Additionally, investigating the integration of multimodal medical imaging data may further improve generalization and robustness across diverse clinical applications. With further refinement, MedVKAN has the potential to advance medical image segmentation, offering efficient, reliable, and scalable solutions for clinical and biomedical applications.

CRedit authorship contribution statement

Hancan Zhu: Writing-original draft, Investigation, Supervision. Jinhao Chen: Methodology, Conceptualization, Software. Guanghua He: Writing-review & editing, Methodology, Supervision.

Declaration of competing interest

The authors declare that they have no competing financial interests.

Acknowledgment

This work was supported by Humanities and Social Science Fund of Ministry of Education of China (23YJAZH232) and Scientific Research Project of Shaoxing University (20210038).

Data availability

All datasets utilized in this study are publicly accessible.

References

- [1] X. Mei *et al.*, "Artificial intelligence-enabled rapid diagnosis of patients with COVID-19," *Nature medicine*, vol. 26, no. 8, pp. 1224-1228, 2020.
- [2] L. Dai *et al.*, "A deep learning system for predicting time to progression of diabetic retinopathy," *Nature Medicine*, vol. 30, no. 2, pp. 584-594, 2024.
- [3] X. Chen *et al.*, "Recent advances and clinical applications of deep learning in medical image analysis," *Medical image analysis*, vol. 79, p. 102444, 2022.
- [4] Y. LeCun, L. Bottou, Y. Bengio, and P. Haffner, "Gradient-based learning applied to document recognition," *Proceedings of the IEEE*, vol. 86, no. 11, pp. 2278-2324, 1998.
- [5] A. Jungo *et al.*, "On the effect of inter-observer variability for a reliable estimation of uncertainty of medical image segmentation," in *Medical Image Computing and Computer Assisted*

Intervention–MICCAI 2018: 21st International Conference, Granada, Spain, September 16-20, 2018, Proceedings, Part I, 2018: Springer, pp. 682-690.

- [6] M. Khened, V. A. Kollerathu, and G. Krishnamurthi, "Fully convolutional multi-scale residual DenseNets for cardiac segmentation and automated cardiac diagnosis using ensemble of classifiers," *Medical image analysis*, vol. 51, pp. 21-45, 2019.
- [7] X. Jiang *et al.*, "End-to-end prognostication in colorectal cancer by deep learning: a retrospective, multicentre study," *The Lancet Digital Health*, vol. 6, no. 1, pp. e33-e43, 2024.
- [8] O. Ronneberger, P. Fischer, and T. Brox, "U-net: Convolutional networks for biomedical image segmentation," in *Medical image computing and computer-assisted intervention–MICCAI 2015: 18th international conference, Munich, Germany, October 5-9, 2015, proceedings, part III 18*, 2015: Springer, pp. 234-241.
- [9] F. Isensee, P. F. Jaeger, S. A. Kohl, J. Petersen, and K. H. Maier-Hein, "nnU-Net: a self-configuring method for deep learning-based biomedical image segmentation," *Nature methods*, vol. 18, no. 2, pp. 203-211, 2021.
- [10] A. Vaswani, "Attention is all you need," *Advances in Neural Information Processing Systems*, 2017.
- [11] A. Dosovitskiy, "An image is worth 16x16 words: Transformers for image recognition at scale," *arXiv preprint arXiv:2010.11929*, 2020.
- [12] K. He, X. Zhang, S. Ren, and J. Sun, "Deep residual learning for image recognition," in *Proceedings of the IEEE conference on computer vision and pattern recognition*, 2016, pp. 770-778.
- [13] A. Myronenko, "3D MRI brain tumor segmentation using autoencoder regularization," in *Brainlesion: Glioma, Multiple Sclerosis, Stroke and Traumatic Brain Injuries: 4th International Workshop, BrainLes 2018, Held in Conjunction with MICCAI 2018, Granada, Spain, September 16, 2018, Revised Selected Papers, Part II 4*, 2019: Springer, pp. 311-320.
- [14] Z. Liu *et al.*, "Swin transformer: Hierarchical vision transformer using shifted windows," in *Proceedings of the IEEE/CVF international conference on computer vision*, 2021, pp. 10012-10022.
- [15] A. Hatamizadeh *et al.*, "Unetr: Transformers for 3d medical image segmentation," in *Proceedings of the IEEE/CVF winter conference on applications of computer vision*, 2022, pp. 574-584.
- [16] A. Hatamizadeh, V. Nath, Y. Tang, D. Yang, H. R. Roth, and D. Xu, "Swin unetr: Swin transformers for semantic segmentation of brain tumors in mri images," in *International MICCAI brainlesion workshop*, 2021: Springer, pp. 272-284.
- [17] A. Sinha and J. Dolz, "Multi-scale self-guided attention for medical image segmentation," *IEEE journal of biomedical and health informatics*, vol. 25, no. 1, pp. 121-130, 2020.
- [18] L. Zhu, X. Wang, Z. Ke, W. Zhang, and R. W. Lau, "Biformer: Vision transformer with bi-level routing attention," in *Proceedings of the IEEE/CVF conference on computer vision and pattern recognition*, 2023, pp. 10323-10333.
- [19] A. Gu, K. Goel, and C. Ré, "Efficiently modeling long sequences with structured state spaces," *arXiv preprint arXiv:2111.00396*, 2021.
- [20] A. Gu *et al.*, "Combining recurrent, convolutional, and continuous-time models with linear state space layers," *Advances in neural information processing systems*, vol. 34, pp. 572-585, 2021.
- [21] A. Gu and T. Dao, "Mamba: Linear-time sequence modeling with selective state spaces," *arXiv*

preprint *arXiv:2312.00752*, 2023.

- [22] L. Zhu, B. Liao, Q. Zhang, X. Wang, W. Liu, and X. Wang, "Vision Mamba: Efficient Visual Representation Learning with Bidirectional State Space Model," in *Forty-first International Conference on Machine Learning*, 2024.
- [23] J. Ma, F. Li, and B. Wang, "U-mamba: Enhancing long-range dependency for biomedical image segmentation," *arXiv preprint arXiv:2401.04722*, 2024.
- [24] Y. Liu *et al.*, "VMamba: Visual State Space Model," *Advances in Neural Information Processing Systems*, 2024.
- [25] J. Liu *et al.*, "Swin-umamba: Mamba-based unet with imagenet-based pretraining," in *International Conference on Medical Image Computing and Computer-Assisted Intervention*, 2024: Springer, pp. 615-625.
- [26] Z. Xing, T. Ye, Y. Yang, G. Liu, and L. Zhu, "Segmamba: Long-range sequential modeling mamba for 3d medical image segmentation," in *International Conference on Medical Image Computing and Computer-Assisted Intervention*, 2024: Springer, pp. 578-588.
- [27] Z. Liu *et al.*, "Kan: Kolmogorov-arnold networks," *arXiv preprint arXiv:2404.19756*, 2024.
- [28] Z. Liu, P. Ma, Y. Wang, W. Matusik, and M. Tegmark, "Kan 2.0: Kolmogorov-arnold networks meet science," *arXiv preprint arXiv:2408.10205*, 2024.
- [29] A. N. Kolmogorov, *On the representation of continuous functions of several variables by superpositions of continuous functions of a smaller number of variables*. American Mathematical Society, 1961.
- [30] V. Tikhomirov, "On the representation of continuous functions of several variables as superpositions of continuous functions of one variable and addition," in *Selected Works of AN Kolmogorov*: Springer, 1991, pp. 383-387.
- [31] C. Li *et al.*, "U-kan makes strong backbone for medical image segmentation and generation," *arXiv preprint arXiv:2406.02918*, 2024.
- [32] X. Yang and X. Wang, "Kolmogorov-arnold transformer," *arXiv preprint arXiv:2409.10594*, 2024.
- [33] A. D. Bodner, A. S. Tepsich, J. N. Spolski, and S. Pourteau, "Convolutional Kolmogorov-Arnold Networks," *arXiv preprint arXiv:2406.13155*, 2024.
- [34] Y. Wu, T. Li, Z. Wang, H. Kang, and A. He, "TransUKAN: Computing-Efficient Hybrid KAN-Transformer for Enhanced Medical Image Segmentation," *arXiv preprint arXiv:2409.14676*, 2024.
- [35] C.-Y. Lee, S. Xie, P. Gallagher, Z. Zhang, and Z. Tu, "Deeply-supervised nets," in *Artificial intelligence and statistics*, 2015: Pmlr, pp. 562-570.
- [36] S. Woo, J. Park, J.-Y. Lee, and I. S. Kweon, "Cbam: Convolutional block attention module," in *Proceedings of the European conference on computer vision (ECCV)*, 2018, pp. 3-19.
- [37] H. Cao *et al.*, "Swin-unet: Unet-like pure transformer for medical image segmentation," in *European conference on computer vision*, 2022: Springer, pp. 205-218.
- [38] J. Ma *et al.*, "The multimodality cell segmentation challenge: toward universal solutions," *Nature methods*, pp. 1-11, 2024.
- [39] J. Ma *et al.*, "Unleashing the strengths of unlabeled data in pan-cancer abdominal organ quantification: the flare22 challenge," *arXiv preprint arXiv:2308.05862*, 2023.
- [40] W. Al-Dhabyani, M. Gomaa, H. Khaled, and A. Fahmy, "Dataset of breast ultrasound images," *Data in brief*, vol. 28, p. 104863, 2020.

- [41] O. Bernard *et al.*, "Deep learning techniques for automatic MRI cardiac multi-structures segmentation and diagnosis: is the problem solved?," *IEEE transactions on medical imaging*, vol. 37, no. 11, pp. 2514-2525, 2018.
- [42] X. Zhao *et al.*, "M2SNet: Multi-scale in multi-scale subtraction network for medical image segmentation," *arXiv preprint arXiv:2303.10894*, 2023.
- [43] M. Jun *et al.*, "COVID-19 CT lung and infection segmentation dataset," (*No Title*), 2020.
- [44] L. Maier-Hein and B. Menze, "Metrics reloaded: Pitfalls and recommendations for image analysis validation," *arXiv.org*, no. 2206.01653, 2022.